Geophysical Research Letters®

RESEARCH LETTER
10.1029/2024GL111263

Tropospheric Thermodynamic Conditions Necessary for Tropical Cyclone Rapid Intensification

Stipo Sentić[1], **Željka Stone**[1,2], **and David J. Raymond**[1,2]

[1]Climate and Weather Consortium, New Mexico Institute of Mining and Technology, Socorro, NM, USA, [2]Physics Department, New Mexico Institute of Mining and Technology, Socorro, NM, USA

Key Points:

- Rapid intensification occurs in a narrow range of atmospheric thermodynamic conditions
- In addition to low wind shear and high SST, low instability index and high saturation fraction are necessary

Supporting Information:

Supporting Information may be found in the online version of this article.

Correspondence to:

S. Sentić,
stipo.sentic@nmt.edu

Citation:

Sentić, S., Stone, Ž., & Raymond, D. J. (2024). Tropospheric thermodynamic conditions necessary for tropical cyclone rapid intensification. *Geophysical Research Letters*, *51*, e2024GL111263. https://doi.org/10.1029/2024GL111263

Received 8 JUL 2024
Accepted 20 OCT 2024

Author Contributions:

Conceptualization: Željka Stone, David J. Raymond
Funding acquisition: Željka Stone
Investigation: Željka Stone, David J. Raymond
Project administration: Željka Stone, David J. Raymond
Software: David J. Raymond
Supervision: Željka Stone, David J. Raymond
Writing – original draft: Željka Stone, David J. Raymond
Writing – review & editing: David J. Raymond

Abstract

As a part of the Tropical Cyclone Rapid Intensification (TCRI) project, we investigated thermodynamic conditions necessary for cyclone intensification. While high sea surface temperature and low tropospheric wind shear are well known environmental factors contributing to storm intensification, they are not sufficient to predict intensification and rapid intensification in particular. To explore thermodynamic factors contributing to intensification, we used dropsondes deployed in pre-storm and storm environments interpolated on a regular grid via a 3D variational analysis. We find that in mesoscale convective areas an instability index, which measures the stability of the atmosphere to moist convection, and saturation fraction, which measures the moisture content of the atmosphere, show a narrow range of values favorable for intensification, and rapid intensification in particular.

Plain Language Summary

It is well known that warm seas and calm winds aloft support rapid development of deadly tropical cyclones–hurricanes. However, storms in those conditions do not always intensify into hurricanes, some of them decay. During the Tropical Cyclone Rapid Intensification (TCRI) project we investigated additional factors which contribute to storm intensification. By analyzing hundreds of dropsondes, instruments which collect profiles of important thermodynamic variables from high in the atmosphere to the ocean surface, we found that in the most stormy part of the hurricane the atmosphere must be in a sweet spot: the temperature of the atmosphere 1–3 km height must be cool enough and the moisture content in the atmosphere must be high enough simultaneously, in order to produce intensification. This finding has repercussions for predicting hurricane development.

1. Introduction

The Tropical Cyclone Rapid Intensification (TCRI) project aims to shed light on mechanisms of tropical cyclone (TC) intensification, specifically rapid intensification (RI). Numerical models fail to predict the onset time and rate of intensification for weak TCs, with a large bias toward intensities lower than observed. TCRI aims at remedying suspected mechanisms missing in numerical weather prediction models by gathering unprecedented amount of observations to identify these mechanisms. This project aims to understand mechanisms missing in numerical weather prediction models. These efforts are closely coordinated with NOAA's Hurricane Research Division (HRD) Advancing the Prediction of Hurricanes Experiment (APHEX) by utilizing two P-3 and one G-IV aircraft together carrying an impressive array of instruments: GPS dropsondes, tail Doppler radar, a stepped frequency microwave radiometer, cloud microphysics probes, the Imaging Wind and Rain Airborne Profiler, the Wide Swath Radar Altimeter, and the Compact rotational Raman Lidar (Doyle et al., 2024).

From 2020 to 2023, missions were flown into different stages of TCs, and numerous modules were deployed to collect data to study these mechanisms through observations and numerical experiments. In numerical experiments, for example, Judt et al. (2023) identified two modes of RI in MPAS simulations; marathon RI, which takes longer to intensify, and sprint, which intensifies rapidly. Finocchio and Rios-Berrios (2021) found that vertical shear impact on RI varies when applied at different stages of the storm in their idealized numerical simulation. On the other hand, observational analysis of tail Doppler radar data in Fischer et al. (2024) showed that RI is favored in storms with weak vortex tilting and low ventilation of storm air, while Richter et al. (2021) showed that the surface drag coefficient used to quantify air–sea momentum transfer is more sensitive and underestimated at hurricane strength surface wind speeds than previously suspected. These and other TCRI studies so far are in agreement with previous observations that a low tropospheric shear and high sea surface temperatures (SSTs) support RI. For example, Kaplan and DeMaria (2003) show that RI storms have 850–200 hPa wind shear mean values around 9.52 kt, compared to non-RI cases with 16.52 kt mean wind shear. Similarly, they found RI cases have mean SST values around 28.4°C, while non-RI cases average lower, at 27.5°C.

In this paper, we explore tropospheric observations of thermodynamic conditions favorable for intensification and RI. We focus on in situ dropsonde data deployed throughout the TCRI campaign, when almost 800 dropsondes were deployed in circumnavigating flight patterns centered on the eye of the TC. We expand this data set with dropsondes from previous field campaigns. The dropsondes collected vertical profiles of temperature, water vapor mixing ratio, pressure, and horizontal wind speed, which we use to produce 3-dimensional variational (3DVar) analyses, which mass-constrain interpolated data, thus enabling us to study thermodynamics favorable for TC intensification.

Previous studies (Gjorgjievska & Raymond, 2014; Raymond et al., 2011) found that saturation fraction, and instability index were critical for influencing spin-up of tropical depressions and cyclogenesis. Saturation fraction is defined as:

$$SF = \frac{\int \rho r dz}{\int \rho r^* dz} \tag{1}$$

where r is the water vapor mixing ratio and ρ the density, with the numerator being precipitable water, and the denominator saturated precipitable water, while the instability index is defined as:

$$II = s^*(1 - 3km) - s^*(5 - 7km) \tag{2}$$

where $s^* = C_p \log\left(\theta_e^*\right)$ is the saturated moist entropy (θ_e^* being the saturated equivalent potential temperature). An inverse relationship was found: low instability index was associated with high saturation fraction. This relationship, called moisture quasi-equilibrium, and its relationship to convection is described in detail in Raymond and Fuchs-Stone (2021). Raymond et al. (2011) and Gjorgjievska and Raymond (2014) showed that the mid-level potential vorticity is crucial for this relationship in cyclogenesis. A strong mid-level potential vorticity maximum was associated with a low instability index. Via the thermal wind gradient balance, a potential vorticity maximum produces warming above and cooling below the maximum, and since the instability index is a function of temperature at a given pressure, this leads to lowering of the instability index.

We look at the saturation fraction–instability index relationship in the context of TC intensification and RI. We use dropsonde data from the TCRI and previous field campaigns to produce 3DVar analysis for 99 flights, and analyze conditions supporting RI. Please refer to Section 2 for details on the 3DVar analyses, and Table S1 for details on each of the 99 3DVars.

Section 2 discusses data and methods. We show thermodynamic relationships discussed above in Section 3, and in Section 4 demonstrate the evolution of these parameters for two contrasting cases. We present our conclusions in Section 5.

2. Data and Methods

We use high altitude Airborne Vertical Atmospheric Profiling System (AVAPS) dropsondes (e.g., Wick et al., 2018) from a number of field campaigns to produce 99 3DVar analyses (see Table S1, for list of cases). The majority of sondes were collected during the TCRI project which contains all 3DVars with RI cases. We emphasize cases which have 24 hr intensification larger than 20 kt (moderately intensifying cases) out of which we single out RI cases, with 24-intensity change greater than 30 kt.

For each high altitude flight into disturbances or storms, data are interpolated onto a regular grid using a 3-dimensional variational analysis (3DVar) with an anelastic mass continuity constraint via a penalty function method (López Carrillo & Raymond, 2011; Raymond & López Carrillo, 2011). All 3DVars have a 0.25° horizontal and 200 m vertical resolution, with a horizontal smoothing appropriate for approximately 1° dropsonde spacing, and minimal vertical smoothing. The effective resolution is that of the dropsonde spacing and the finer grid resolution is employed to produce numerically smooth fields. No numerical model derived background field is used in the 3DVars. Also, while a lot of the flights contained synoptic surveillance regions, we limit our analyses to the regions closest to the main circulation, that is, with averaging box center within 3.5° from the

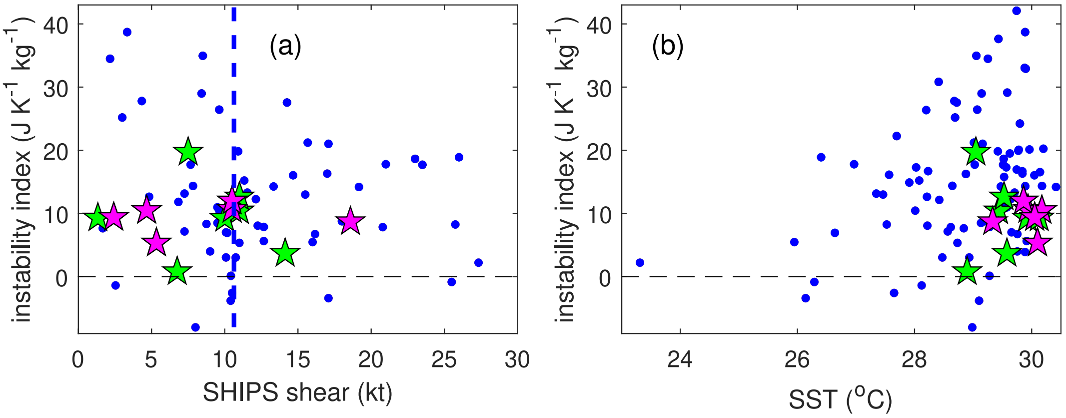

Figure 1. Thermodynamic relationships between (a) instability index and SHIPS shear, and (b) instability index and SST. Moderately intensifying cases are denoted with green stars, out of which RI cases are marked with magenta stars. Dashed vertical blue line in panel a is the mean environmental shear value for all RI cases between the years 1982–2020 using the SHIPS database (Stone et al., 2023).

absolute vorticity maximum (with all moderately intensifying and RI cases within 2°). Averages used in this study are produced in 2 by 2° boxes centered on 4 km mass flux maxima with positive mass flux throughout the troposphere. Table S1 shows details for each 3DVar: reference time, averaging box coordinates, field campaign, and storm speed at the time of the dropsonde deployment. We also use the Statistical Hurricane Intensity Prediction Scheme (SHIPS, DeMaria et al., 2022) 850–200-hPa vertical wind shear magnitude, and the National Oceanic and Atmospheric Administration optimally interpolated SSTs (Reynolds et al., 2007). For storm intensity, we use the revised Atlantic hurricane database (HURDAT2, Landsea & Franklin, 2013).

3. Thermodynamic and Environmental Relationships

We compare the instability index with environmental shear and SST favorable for RI in Figure 1. We mark moderately intensifying and RI cases, with greater than 20 and 30 kt maximum sustained winds change, with green and magenta stars, respectively.

Instability index versus SHIPS shear, Figure 1a, shows that most of the moderately intensifying and RI cases have shear about the climatological mean for RI cases, and lower, with a couple of cases with higher shear. This moderately low shear seems to support the intensification of these cases in agreement with previous research (Gray, 1968; Kaplan & DeMaria, 2003; Kaplan et al., 2015; Ryglicki et al., 2018; Tao & Zhang, 2015). Instability index and SST, however, shown in Figure 1b, reveal a striking relationship. While it is well known that high SSTs support intensification of TCs (Kaplan & DeMaria, 2003; Majumdar et al., 2023), in this figure we see the importance of instability index for intensification: a narrow range of instability index and SSTs support moderately intensifying and RI cases.

While high SST values are necessary for strongly intensifying and RI cases, many non-intensifying cases with a high instability index and high SST show that those conditions are not sufficient. In particular, most cases with high SST but instability index greater than 15 J K^{-1} kg^{-1} lack strong intensification or RI.

Figure 2a shows the saturation fraction–instability index anti-correlation ($r = -0.67$) mentioned in the introduction. Low instability index is associated with high saturation fraction in mesoscale convective regions. Moderately intensifying and RI cases occupy a narrow region of Figure 2a, with a low instability index and high saturation fraction. RI cases seem to occupy an even narrower space, about 5–12 J K^{-1} kg^{-1} instability index, and about 0.85–0.91 saturation fraction. These seem to be necessary but not sufficient conditions for RI to occur, as evidenced by RI cases being surrounded by non-RI cases in this region of favorable conditions.

The moisture quasi-equilibrium relationship we just showed, relates the stability and moisture content of an atmospheric column, and was shown to exist both in observations (Fuchs-Stone et al., 2020; Gjorgjievska & Raymond, 2014; Raymond et al., 2011, 2014; Sentić et al., 2015; Sessions et al., 2019) and numerical simulations of convection (Raymond & Flores, 2016; Raymond & Sessions, 2007; Sentić & Sessions, 2017; Sentić

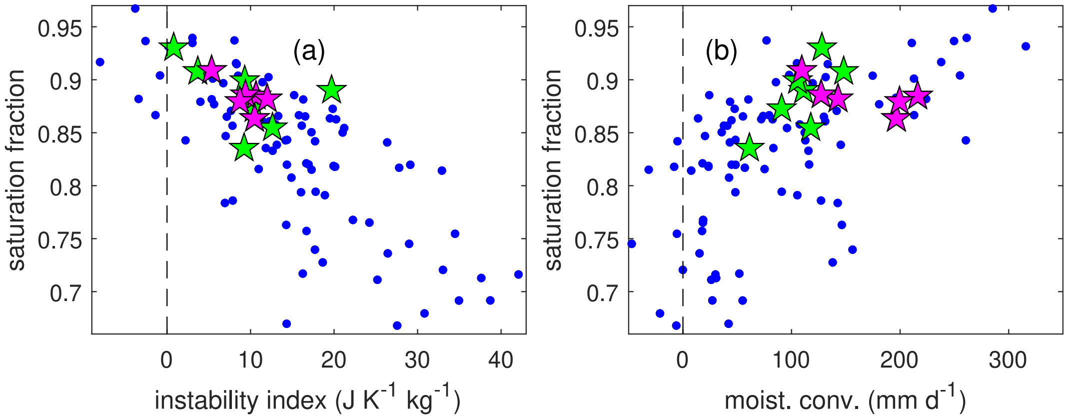

Figure 2. Thermodynamic relationships between (a) saturation fraction and instability index, and (b) saturation fraction and moisture convergence. Symbols are explained in Figure 1.

et al., 2015; Sessions et al., 2015, 2016). The moisture quasi-equilibrium mechanism posits that the increase in saturation fraction at low instability indices is related to the mass flux, ρw, where ρ is the density and w the vertical velocity. We can also relate the mass flux to moisture convergence:

$$S_{mr} = -\int \nabla_h \cdot (\rho \mathbf{v}_h r)\, dz \tag{3}$$

where subscript h denotes the horizontal component, $\mathbf{v}$ is the wind velocity, ρ is the density, and r is the mixing ratio. A stronger and more bottom heavy mass flux profile concentrates import of moisture at lower levels where it is more abundant. Figure 2b shows saturation fraction as a function of moisture convergence. In general, high saturation fraction is associated with high moisture convergence. As in Figure 2a, intensification is constrained to a narrow range of saturation fraction, and a relatively moderate range of moisture convergence.

The importance of the above results is also highlighted in the potential vorticity as the source of instability index changes, as explained in the introduction. Figure 3 shows the instability index as a function of the 5–7 km potential vorticity for all the 3DVars. Instability index is anti-correlated with the mid-level potential vorticity as expected from previous research. A mid-level potential vorticity maximum leads to warming above and cooling below which decreases the instability index. The range of phase space with moderate intensification and RI is limited to a critical range of 1–3 potential vorticity units (pvu, 10^{-6} m^{-2} s^{-1} K kg^{-1}), with values outside this range not supporting intensification.

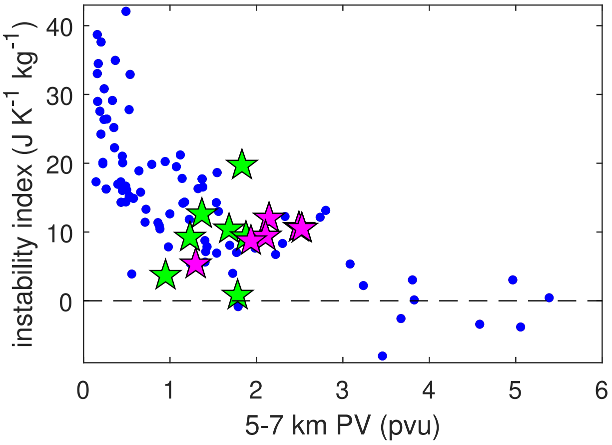

Figure 3. Thermodynamic relationship between instability index and mid-level potential vorticity. Symbols are explained in Figure 1.

Finally, we can look at vertical profiles of the above thermodynamic parameters in two regions of the saturation fraction–instability index phase space. A region of conditions favorable for intensification and RI, with instability index 5–12 J K^{-1} kg^{-1}, and saturation fraction 0.85–0.91, is shown in red in Figure 4. A second region with non-favorable conditions, with instability index greater than 20 J K^{-1} kg^{-1}, and saturation fraction less than 0.8 is shown in black in Figure 4. The region of phase space favorable for RI shows a mid-level potential vorticity maximum (Figure 4a), compared to a weak potential vorticity with a low level maximum for the non-favorable phase space. This is reflected in the saturated moist entropy (Figure 4b) from which the instability index is deduced, showing a cooling below and warming above the potential vorticity mid-level maximum. The lower instability index leads to stronger bottom heavy mass flux profile in the phase space favorable for intensification and RI (Figure 4c), which leads to increased moisture convergence leading to the moistening of the column as seen in increased moist entropy (Figure 4d).

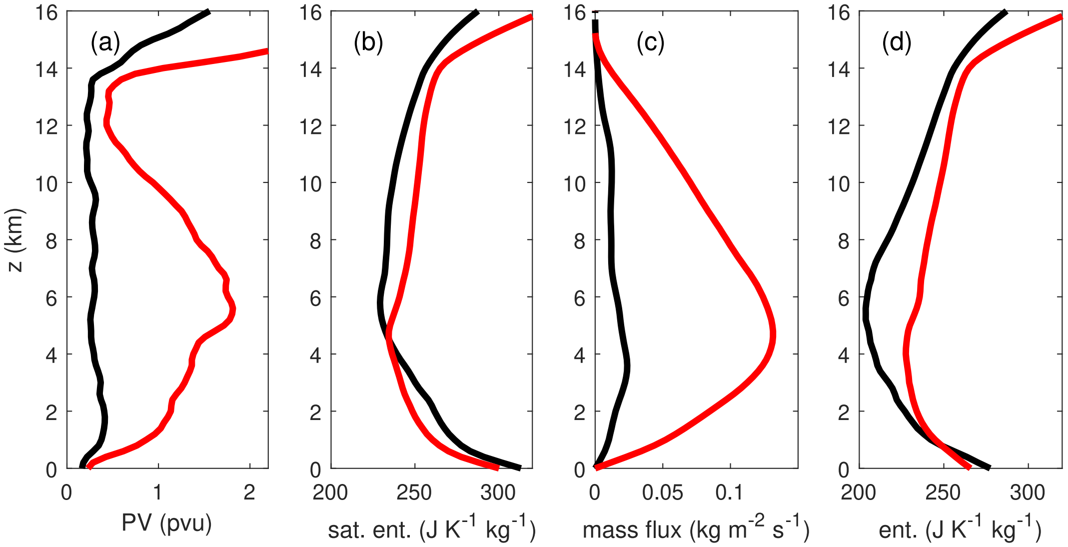

Figure 4. Average thermodynamic profiles of (a) potential vorticity, (b) saturated moist entropy, (c) mass flux, and (d) moist entropy, for regions of saturation fraction–instability index phase space favorable and non-favorable of RI in red and black, respectively. The favorable region average profile has saturation fraction 0.88 and instability index 8.63 J K^{-1} kg^{-1}, and the non-favorable region average profile has saturation fraction 0.72 and instability index 31.26 J K^{-1} kg^{-1}.

Next, we look at two contrasting cases: Ian (2022), and Gaston (2010). Both storms started in the favorable region of the saturation fraction–instability index phase space, but had different outcomes: Ian rapidly intensified, while Gaston decayed.

4. Time Evolution of Two Contrasting Cases: Ian (2022) and Gaston (2010)

Hurricane Ian (2022) was a rapidly intensifying storm which was well observed with 7 G-IV flights, out of which we use 5 flights which produced dropsonde grids amicable to the 3DVar analysis. Gaston was a brief tropical storm which decayed, and was observed with 7 high latitude flights with different missions (see Table S1). Figure 5 shows time series of thermodynamic variables for Ian (left, panels a, c, e, and g) and Gaston (right, panels b, d, f, and h).

In Figures 5a and 5b the HURDAT2 maximum sustained wind speed shows intensification of Ian over 60 kt in 1.5 days, with a steady 30 kt for Gaston. The decrease of minimum pressure shows the same for Ian, while Gaston has a steady high pressure. It is well known that high SSTs and low shear contribute to the development of TCs (e.g., Gray, 1968; Kaplan & DeMaria, 2003; Kaplan et al., 2015; Majumdar et al., 2023; Ryglicki et al., 2018; Tao & Zhang, 2015). The Reynolds SST shows steady high values, 30°C, for the intensifying Ian, and almost 2° cooler values at the onset of Gaston (Figures 5c and 5d), with increased, more favorable values for storm intensification, later around days 4–6. The SHIPS shear (blue line in Figures 5c and 5d) lowers during intensification for Ian, relative to the climatological mean (dashed blue line in Figures 5c and 5d), while Gaston shows values comparable to the climatological mean.

Potential vorticity shows non-monotonic increase across the TC–hurricane transition (Figures 5e and 5f, black line) for Ian, and a non-monotonic decrease for Gaston. For Ian, the instability index remains low (red line in panels e–f), around 10 J K^{-1} kg^{-1}, while for Gaston it increases from around 10 to 40 J K^{-1} kg^{-1} during decay. Saturation fraction also starts at high values for both Ian and Gaston (Figures 5g and 5h), but increases to very high values around 0.9 for Ian, and decreases to very low values around 0.7 for Gaston (note that small changes in saturation fraction lead to large changes in convective behavior).

In summary, in Ian the strong mid-level potential vorticity causes a strong temperature dipole which is observed in the low instability index. The low instability index modifies the nature of convection, making it more bottom heavy and stronger. Increase in the slope of the mass flux profile near the surface acts to increase the convergence at those levels, leading to import of moisture and increase in saturation fraction. Gaston behaved in an opposite

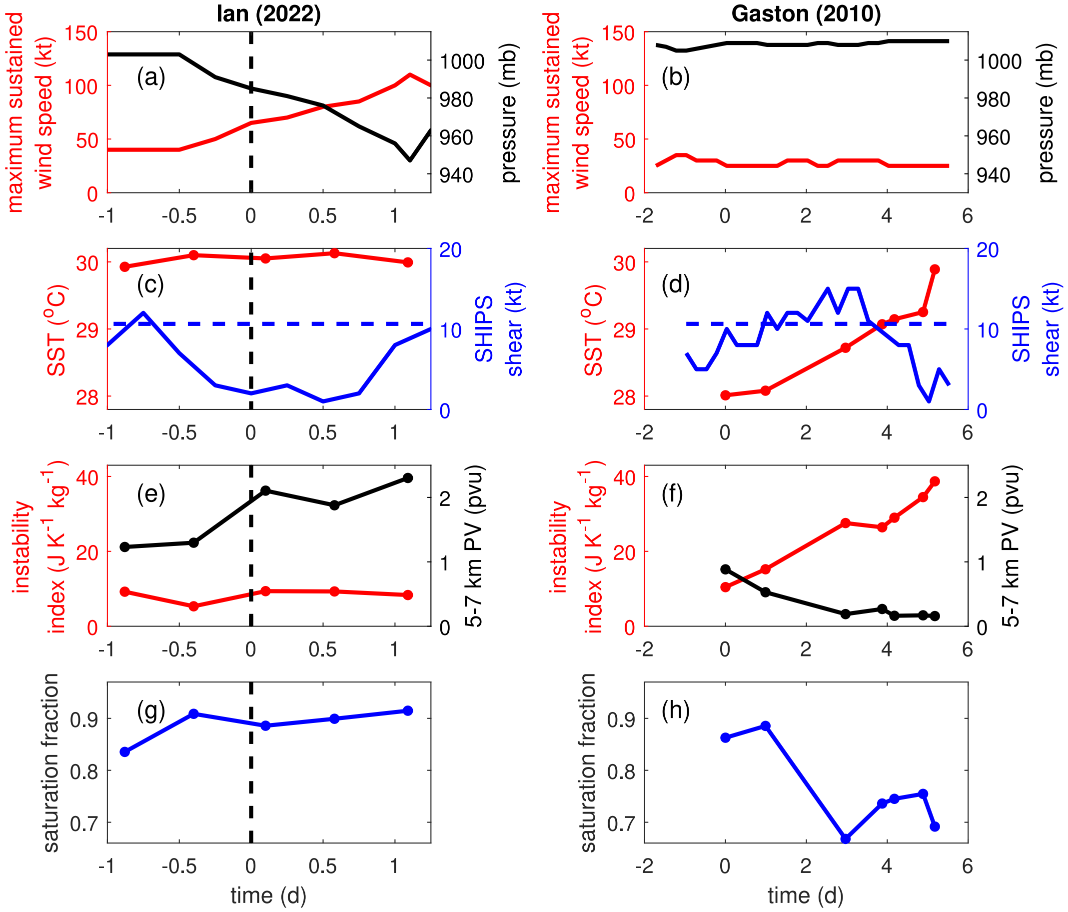

Figure 5. Time series of (a) and (b) HURDAT2 maximum sustained wind speed and minimum pressure, (c and d) Reynolds SST and SHIPS database 200–800 hPa shear, (e and f) 5–7 km potential vorticity, and instability index, and (g and h) saturation fraction, for the five Ian (2022) high altitude flights on the left (panels a, c, e, and g), and for the seven Gaston (2010) high altitude flights on the right (panels b, d, f, and h). Dashed horizontal blue line in panels (c) and (d) is the mean environmental value for all RI cases between the years 1982–2020 using the SHIPS database (Stone et al., 2023). The black vertical dashed line, for Ian, denotes the tropical storm to hurricane transition, with indicated time being relative to this transition.

manner. The ever weakening potential vorticity in the mid-levels was accompanied with increase in instability index and decrease in saturation fraction, a weakening in the mass flux, and export of moisture which contributed to the decay of Gaston.

In Figure 2a, both Ian and Gaston started in the region of the saturation fraction–instability index phase space favorable to intensification, that is, with low instability index and high saturation fraction, in the region with moderately intensifying and RI cases. Ian remained in that region of the phase space, while Gaston migrated toward high instability index and low saturation fraction. The two cases, however, started in different regions of the instability index–SST phase space (Figure 1b), with Ian starting and staying in the region favorable for intensification and RI: low instability index and high SST. Gaston started with a much lower SST, outside of the phase space region of the favorable conditions and evolved clockwise around it into the region with high instability index and SST, which does not support intensification.

5. Conclusions

In this letter we presented the most recent thermodynamic 3DVar analysis of AVAPS dropsonde data collected during the 2020–2023 hurricane seasons, augmented with analyses from previous field campaigns. We used these 3DVars to find environmental and thermodynamic variables which support RI of TCs. While well known factors favorable for TC development, high SST and low tropospheric shear, were present, they were not sufficient for many cases to intensify. However, tropospheric thermodynamic conditions, instability index and saturation fraction in particular, calculated from the 3DVar analyses, support RI of TCs. A narrow range of instability index, about 5–12 J K^{-1} kg^{-1}, and high saturation fraction, about 0.85–0.91, showed cases with RI. As a source of low instability index we showed strong potential vorticity maxima at mid-levels, which, via thermal wind gradient balance, produce a temperature dipole which lowers the instability index. Furthermore, as Raymond and Fuchs-Stone (2021) showed, low instability index leads to high values of saturation fraction due to its effect on convection; an expression of moisture quasi-equilibrium. Compared to intensifying cases, RI cases have a narrower region of favorable conditions with respect to instability index, saturation fraction, SST, and, in some cases, stronger moisture convergence and mid-level PV.

Even though they started in the region of favorable saturation fraction–instability index conditions, rapidly intensifying Ian (2022), and decaying Gaston (2010) showed markedly different evolutions. Gaston had low sea surface temperatures at a low instability index in the beginning stages, which potentially led to the decay. These examples illustrate the potential of using the saturation fraction–instability index, and instability index–SST phase spaces for monitoring the evolution of TC intensification in observations and numerical experiments.

The above leads us to conclude that the narrow region of the saturation fraction–instability index phase space in the convecting region of a developing TC needs to be added to the list of necessary conditions for TC intensification. This result is in agreement with Raymond and Fuchs-Stone (2021) who found that a similar narrow region of the saturation fraction–instability index phase space showed strongest moisture convergence, indicating a possible supporting mechanism for TC intensification.

Though we have only 11 cases of rapid and near-rapid intensification, these cases are tightly clustered in Figures 2 and 3 and in Figure 1b, suggesting that the results are robust. The points in Figure 1a are not as clustered, indicating that SHIPS wind shear is a less discriminating predictor of rapid intensification in our data set; further studies with finer radial range for shear calculation (e.g., Dai et al., 2021; Ryglicki et al., 2018; Shi & Chen, 2021), and tilt of the storm, are left for future work. Future case studies would provide additional tests of our conclusions.

Data Availability Statement

A comprehensive explanation and scripts for downloading the publicly available data, compiling the 3DVar analyses, analyzing the data, and producing the plots, can be found in Sentić (2024). The SST data can be found in Huang et al. (2020). These GPS-dropsonde data are provided courtesy of the NOAA/AOML/Hurricane Research Division in Miami, FL (USA). Dropsonde data for the HS3, PREDICT, and GRIP field campaigns can be obtained in UCAR/NCAR-Earth Observing Laboratory (2016a, 2016b, 2016c, 2017). The SHIPS and HURDAT2 data used in this study and the scripts used to obtain them from operational websites are also found in Sentić (2024). The open source Candis software used to produce the 3DVars can be found in Raymond (2021).

Acknowledgments

We thank Carlos López Carillo and Julio Marín for useful discussions. We also thank two anonymous reviewers for constructive and insightful reviews. This work was supported by the Office of Naval Research Grant N000142012135.

References

Dai, Y., Majumdar, S. J., & Nolan, D. S. (2021). Tropical cyclone resistance to strong environmental shear. *Journal of the Atmospheric Sciences*, *78*(4), 1275–1293. https://doi.org/10.1175/JAS-D-20-0231.1

DeMaria, M., Franklin, J. L., Zelinsky, R., Zelinsky, D. A., Onderlinde, M. J., Knaff, J. A., et al. (2022). The national hurricane center tropical cyclone model guidance suite. *Weather and Forecasting*, *37*(11), 2141–2159. https://doi.org/10.1175/WAF-D-22-0039.1

Doyle, J. D., Dunion, J. P., Rogers, R. F., Finocchio, P. M., Moskaitis, J. R., & Stern, D. P., & Cossuth, J. (2024). Overview of the tropical cyclone rapid intensification (TCRI) program. In *36th conference on hurricanes and tropical meteorology*.

Finocchio, P. M., & Rios-Berrios, R. (2021). The intensity- and size-dependent response of tropical cyclones to increasing vertical wind shear. *Journal of the Atmospheric Sciences*, *78*(11), 3673–3690. https://doi.org/10.1175/JAS-D-21-0126.1

Fischer, M. S., Rogers, R. F., Reasor, P. D., & Dunion, J. P. (2024). An observational analysis of the relationship between tropical cyclone vortex tilt, precipitation structure, and intensity change. *Monthly Weather Review*, *152*(1), 203–225. https://doi.org/10.1175/MWR-D-23-0089.1

Fuchs-Stone, Ž., Raymond, D. J., & Sentić, S. (2020). OTREC2019: Convection over the East Pacific and southwest Caribbean. *Geophysical Research Letters*, *47*(11), e2020GL087564. https://doi.org/10.1029/2020GL087564

Gjorgjievska, S., & Raymond, D. J. (2014). Interaction between dynamics and thermodynamics during tropical cyclogenesis. *Atmospheric Chemistry and Physics*, *14*(6), 3065–3082. https://doi.org/10.5194/acp-14-3065-2014

Gray, W. M. (1968). Global view of the origin of tropical disturbances and storms. *Monthly Weather Review*, *96*(10), 669–700. https://doi.org/10.1175/1520-0493(1968)096⟨0669:GVOTOO⟩2.0.CO;2

Huang, B., Liu, C., Banzon, V. F., Freeman, E., Graham, G., Hankins, W., et al. (2020). *NOAA 0.25-degree daily optimum interpolation sea surface temperature (OISST), version 2.1*. NOAA National Centers for Environmental Information. https://doi.org/10.25921/RE9P-PT57

Judt, F., Rios-Berrios, R., & Bryan, G. H. (2023). Marathon versus sprint: Two modes of tropical cyclone rapid intensification in a global convection-permitting simulation. *Monthly Weather Review*, *151*(10), 2683–2699. https://doi.org/10.1175/MWR-D-23-0038.1

Kaplan, J., & DeMaria, M. (2003). Large-scale characteristics of rapidly intensifying tropical cyclones in the North Atlantic basin. *Weather and Forecasting*, *18*(6), 1093–1108. https://doi.org/10.1175/1520-0434(2003)018⟨1093:LCORIT⟩2.0.CO;2

Kaplan, J., Rozoff, C. M., DeMaria, M., Sampson, C. R., Kossin, J. P., Velden, C. S., et al. (2015). Evaluating environmental impacts on tropical cyclone rapid intensification predictability utilizing statistical models. *Weather and Forecasting*, *30*(5), 1374–1396. https://doi.org/10.1175/WAF-D-15-0032.1

Landsea, C., & Franklin, J. (2013). Atlantic hurricane database uncertainty and presentation of a new database format. *Monthly Weather Review*, *141*(10), 3576–3592. https://doi.org/10.1175/MWR-D-12-00254.1

López Carrillo, C., & Raymond, D. J. (2011). Retrieval of three-dimensional wind fields from Doppler radar data using an efficient two-step approach. *Atmospheric Measurement Techniques*, *4*(12), 2717–2733. https://doi.org/10.5194/amt-4-2717-2011

Majumdar, S. J., Nebylitsa, S., Klotzbach, P. J., Masiello, C., & Michael, Z. R. (2023). North Atlantic tropical cyclone intensification: Regional drivers and trends. *Geophysical Research Letters*, *50*(17), e2023GL104803. https://doi.org/10.1029/2023GL104803

Raymond, D. J. (2021). *Candis*. Zenodo. https://doi.org/10.5281/ZENODO.5150519

Raymond, D. J., & Flores, M. M. (2016). Predicting convective rainfall over tropical oceans from environmental conditions. *Journal of Advances in Modeling Earth Systems*, *8*(2), 703–718. https://doi.org/10.1002/2015MS000595

Raymond, D. J., & Fuchs-Stone, Ž. (2021). Emergent properties of convection in OTREC and PREDICT. *Journal of Geophysical Research: Atmospheres*, *126*(4), e2020JD033585. https://doi.org/10.1029/2020JD033585

Raymond, D. J., Gjorgjievska, S., Sessions, S. L., & Fuchs, Ž. (2014). Tropical cyclogenesis and mid-level vorticity. *Australian Meteorological and Oceanographic Journal*, *64*(1), 11–25. https://doi.org/10.22499/2.6401.003

Raymond, D. J., & López Carrillo, C. (2011). The vorticity budget of developing typhoon Nuri (2008). *Atmospheric Chemistry and Physics*, *11*(1), 147–163. https://doi.org/10.5194/acp-11-147-2011

Raymond, D. J., & Sessions, S. L. (2007). Evolution of convection during tropical cyclogenesis. *Geophysical Research Letters*, *34*(6), L06811. https://doi.org/10.1029/2006GL028607

Raymond, D. J., Sessions, S. L., & López Carrillo, C. (2011). Thermodynamics of tropical cyclogenesis in the northwest Pacific. *Journal of Geophysical Research*, *116*(D18), D18101. https://doi.org/10.1029/2011JD015624

Reynolds, R. W., Smith, T. M., Liu, C., Chelton, D. B., Casey, K. S., & Schlax, M. G. (2007). Daily high-resolution-blended analyses for sea surface temperature. *Journal of Climate*, *20*(22), 5473–5496. https://doi.org/10.1175/2007JCLI1824.1

Richter, D. H., Wainwright, C., Stern, D. P., Bryan, G. H., & Chavas, D. (2021). Potential low bias in high-wind drag coefficient inferred from dropsonde data in hurricanes. *Journal of the Atmospheric Sciences*, *78*(7), 2339–2352. https://doi.org/10.1175/JAS-D-20-0390.1

Ryglicki, D. R., Cossuth, J. H., Hodyss, D., & Doyle, J. D. (2018). The unexpected rapid intensification of tropical cyclones in moderate vertical wind shear. Part I: Overview and observations. *Monthly Weather Review*, *146*(11), 3773–3800. https://doi.org/10.1175/MWR-D-18-0020.1

Sentić, S. (2024). Thermodynamics of rapid intensification [Dataset]. *Zenodo*. https://doi.org/10.5281/ZENODO.12616411

Sentić, S., & Sessions, S. L. (2017). Idealized modeling of convective organization with changing sea surface temperatures using multiple equilibria in weak temperature gradient simulations. *Journal of Advances in Modeling Earth Systems*, *9*(2), 1431–1449. https://doi.org/10.1002/2016MS000873

Sentić, S., Sessions, S. L., & Fuchs, Ž. (2015). Diagnosing DYNAMO convection with weak temperature gradient simulations. *Journal of Advances in Modeling Earth Systems*, *7*(4), 1849–1871. https://doi.org/10.1002/2015MS000531

Sessions, S. L., Herman, M. J., & Sentić, S. (2015). Convective response to changes in the thermodynamic environment in idealized weak temperature gradient simulations. *Journal of Advances in Modeling Earth Systems*, *7*(2), 712–738. https://doi.org/10.1002/2015MS000446

Sessions, S. L., Sentić, S., & Herman, M. J. (2016). The role of radiation in organizing convection in weak temperature gradient simulations. *Journal of Advances in Modeling Earth Systems*, *8*(1), 244–271. https://doi.org/10.1002/2015MS000587

Sessions, S. L., Sentić, S., & Raymond, D. J. (2019). Balanced dynamics and moisture quasi-equilibrium in dynamo convection. *Journal of the Atmospheric Sciences*, *76*(9), 2781–2799. https://doi.org/10.1175/JAS-D-18-0173.1

Shi, D., & Chen, G. (2021). The implication of outflow structure for the rapid intensification of tropical cyclones under vertical wind shear. *Monthly Weather Review*, *149*(12), 4107–4127. https://doi.org/10.1175/MWR-D-21-0141.1

Stone, Ž., Alvey, G. R., Dunion, J. P., Fischer, M. S., Raymond, D. J., Rogers, R. F., et al. (2023). Thermodynamic contribution to vortex alignment and rapid intensification of hurricane sally (2020). *Monthly Weather Review*, *151*(4), 931–951. https://doi.org/10.1175/MWR-D-22-0201.1

Tao, D., & Zhang, F. (2015). Effects of vertical wind shear on the predictability of tropical cyclones: Practical versus intrinsic limit. *Journal of Advances in Modeling Earth Systems*, *7*(4), 1534–1553. https://doi.org/10.1002/2015MS000474

UCAR/NCAR-Earth Observing Laboratory. (2016a). *HS3 2013 Global Hawk dropsonde data. Version 5.0*. UCAR/NCAR—Earth Observing Laboratory. https://doi.org/10.5065/D6736P31

UCAR/NCAR-Earth Observing Laboratory. (2016b). *HS3 2014 Global Hawk dropsonde data. Version 3.0*. UCAR/NCAR—Earth Observing Laboratory. https://doi.org/10.5065/D6GB2243

UCAR/NCAR-Earth Observing Laboratory. (2016c). *NSF/NCAR GV dropsonde data. Version 3.0*. UCAR/NCAR—Earth Observing Laboratory. https://doi.org/10.5065/D6R78CD4

UCAR/NCAR-Earth Observing Laboratory. (2017). *GRIP: NASA DC-8 NCAR/EOL dropsonde data. Version 3.0*. UCAR/NCAR - Earth Observing Laboratory. https://doi.org/10.5065/D6VX0DRT

Wick, G. A., Hock, T. F., Neiman, P. J., Vömel, H., Black, M. L., & Spackman, J. R. (2018). The NCAR–NOAA global hawk dropsonde system. *Journal of Atmospheric and Oceanic Technology*, *35*(8), 1585–1604. https://doi.org/10.1175/JTECH-D-17-0225.1